Numerical Heat Transfer, Part A, 58: 429–456, 2010

ISSN: 1040-7782 print/1521-0634 online
DOI: 10.1080/10407782.2010.508434

Taylor & Francis
Taylor & Francis Group

A TURBULENT IMPINGING JET ON A PLATE COVERED WITH A POROUS LAYER

Cleges Fischer and Marcelo J. S. de Lemos
Departamento de Energia—IEME, Instituto Tecnológico de Aeronáutica—ITA, São José dos Campos, São Paulo, Brazil

This work shows numerical results for a turbulent jet impinging against a flat plane covered with a layer of permeable material, which is kept at a higher temperature than that of the incoming fluid. Parameters such as porosity, permeability, thickness, and thermal conductivity of the porous layer are varied in order to analyze their effects on the local distribution of Nu. The macroscopic equations for mass, momentum, and energy are obtained based on volume-average concept. The numerical technique employed for discretizing the governing equations was the control volume method with a boundary-fitted nonorthogonal coordinate system. The SIMPLE algorithm was used to handle the pressure–velocity coupling. Results indicate that inclusion of a porous layer decreases the peak in Nu avoiding excessive heating or cooling at the stagnation point. Also found, was that the integral heat flux from the wall is enhanced for certain ranges of values of porosity, layer thickness, and thermal conductivity ratio.

1. INTRODUCTION

Turbulent impinging jets are mainly used in industrial applications with the objective of obtaining effective heating, cooling, or drying processes. The main advantage of using impinging jets is the possibility to obtain highly localized mass and heat transfer rates due to thin boundary layers inside of the stagnation region. Applications of such systems include electronics cooling, glass tempering, metals cooling, drying of textiles products and paper, to mention a few.

Published results are mainly concentrated on impinging jets under high mass flow conditions, which reaches an uncovered surface. Pioneering studies considering two-dimensional impinging jets with low Reynolds number, also onto uncovered flat walls, are presented in Gardon and Akfirat [1], who experimentally obtained local and averaged heat transfer coefficients. Sparrow and Wong [2] made use of the well-known heat and mass transfer analogy and took experimental data on local mass transfer for a two-dimensional impinging jet. Results were then converted to heat transfer using the mentioned technique. Chen et al. [3] experimentally and

Received 4 May 2010; accepted 22 June 2010.
The authors are thankful to CNPq and FAPESP for their financial support during the preparation of this work.
Address correspondence to Marcelo J. S. de Lemos, Departamento de Energia—IEME, Instituto Tecnológico de Aeronáutica—ITA, 12228-900—São José dos Campos – SP, Brazil. E-mail: delemos@ita.br

NOMENCLATURE

A_i	macroscopic interface area between the porous region and the clear flow
B	jet width
c_F	Forchheimer coefficient
Da	Darcy number, $\mathrm{Da} = K/H^2$
H	channel height
h	porous layer thickness, film coefficient
K	permeability
k_{eff}	effective thermal conductivity
k	thermal conductivity
L	channel length
Nu	Nusselt number
p	thermodynamic pressure
q_w	integral wall heat flux
q_w^{ϕ}	integral wall heat flux will porous layer
$\langle p \rangle^i$	intrinsic (fluid) average of pressure p
Re	Reynolds number based on the jet width, $\mathrm{Re} = \rho \nu_0 B/\mu$
S_{φ}	source term
T	temperature
$\langle \mathbf{u} \rangle^i$	intrinsic (fluid) average of $\mathbf{u}$
$\mathbf{u}_D$	Darcy velocity vector (volume average over $\mathbf{u}$) $= \phi \langle \mathbf{u} \rangle^i$
x, y	Cartesian coordinates
μ	dynamic viscosity
ρ	density
ν	kinematic viscosity
ϕ	related to porous medium

Subscripts

s,f	solid, fluid
w	wall
o	inlet conditions

numerically analyzed mass and heat transfer induced by a two-dimensional laminar jet. Chiriac and Ortega [4] performed numerical simulations in steady and transitory regime for a two-dimensional jet impinging against a plate with constant temperature. In addition, in recent years a number of research papers covered a wide range of studies in porous media [5–18], including flows parallel to a layer of porous material [19] and across permeable baffles [20, 21] and porous inserts [22]. Investigation on configurations concerning perpendicular jets into a porous core is much needed for optimization of heat sinks attached to solid surfaces. However, studies of porous medium under impinging jets are, unfortunately, yet scarce in the literature. An example found are those given by numerical simulations of Kim and Kuznetsov [23], who investigated optimal characteristics of impinging jets into heat sinks. Other innovative applications of impinging jets, such as fiber hydroentalglement, can also be found in recent literature [24, 25].

As mentioned, for the specific case here investigated, i.e., an impinging jet over a covered plate, there are not too many results in the open literature. One example is the work of Prakash et al. [26, 27], who obtained a flow visualization of turbulent jets impinging against a porous medium. Also, Fu and Huang [28] evaluated the thermal performance of different porous layers under an impinging jet, and Jeng and Tzeng [29] studied the hydrodynamic and thermal performance of a jet impinging on a metallic foam. Recently, Graminho and de Lemos [30] investigated the flow structure of a turbulent jet impinging on a layer of porous material. In reference [30], the macroscopic mathematical model described in detail by de Lemos [31] was applied. Previously, Rocamora and de Lemos [32] had added thermal modeling for the treatment of a permeable medium. Later, the work on isothermal impinging jets was extended to involve thermal analysis [33], but therein only laminar heat transfer was investigated.

The objective of the present contribution is to extend the thermal analysis of laminar regime presented in reference [33] to turbulent flows in order to evaluate

under which circumstances the addition of a porous layer made of thermal conducting material can enhance or damp the overall heat transferred from a flat surface under a turbulent impinging jet.

2. PROBLEM INVESTIGATED

The cases considered here are detailed in Figure 1*a*. A laminar jet with uniform velocity v_o and constant temperature T_o enters through a gap into a channel with height H and length $2L$. Fluid impinges normally against the bottom plate, yielding a two-dimensional confined impinging jet configurarion. The width of the inlet nozzle is B and the bottom plate temperature T_1 is maintained constant and 10 K above the temperature of the incoming jet, T_o. In a different configuration, the bottom surface is covered with a porous layer of height h (Figure 1*b*). In both cases, the flow is assumed to be two-dimensional, turbulent incompressible, and steady. Also, the porous medium is taken to be homogeneous, rigid, and inert. Fluid properties are constant and gravity effects are neglegted.

The boundary conditions for the problem are: (1) constant velocity and temperature profiles of the entering jet, (2) no slip condition on the walls, (3) symmetry condition in $x = 0$, and (4) fully developed flow at channel exit ($x = L$). At the bottom plate ($y = H$), a constant temperature condition is assumed whereas along the upper wall, for $B/2 < x \leq L$, null heat flux condition prevails.

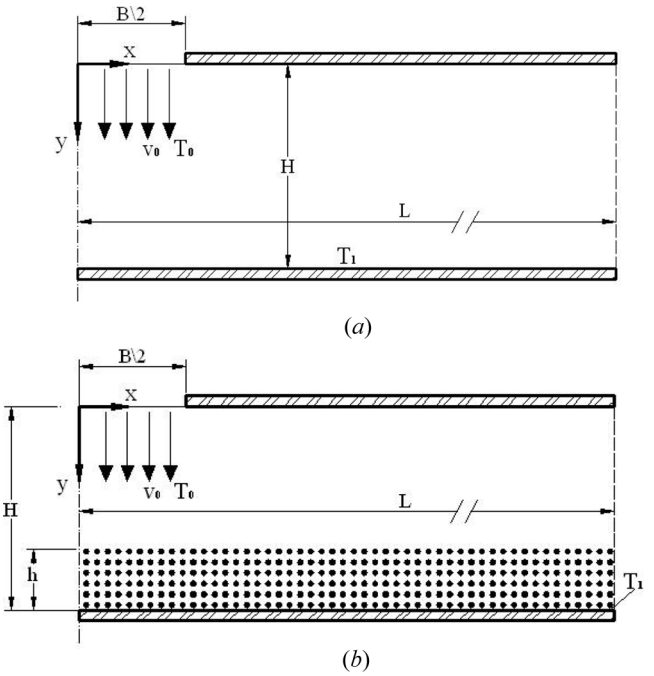

Figure 1. Cases investigated: (*a*) Confined impinging jet on a flat plate—clear medium case and (*b*) confined impinging jet on a plate covered with a layer of porous material—porous case.

3. MATHEMATICAL MODELING

As mentioned, the flow model employed here is described in Graminho and de Lemos [30], whereas thermal modeling is detailed in reference [32], including the energy equation for heat transfer calculations. Therein, details can be found. As most of the theoretical development is readily available in the open literature, the governing equations will just be presented, and details about their derivations can be obtained in the mentioned papers. Essentially, local instantaneous equations are volume-averaged using appropriate mathematical tools [34, 35].

Local Instantaneous Transport Equations

The governing equations for the flow and energy for an incompressible fluid are given by

Continuity

$$\nabla \cdot \mathbf{u} = 0 \tag{1}$$

Momentum

$$\rho\left[\frac{\partial \mathbf{u}}{\partial t} + \nabla \cdot (\mathbf{u}\mathbf{u})\right] = -\nabla p + \mu \nabla^2 \mathbf{u} \tag{2}$$

Energy–fluid phase

$$(\rho c_p)_f \left\{\frac{\partial T_f}{\partial t} + \nabla \cdot (\mathbf{u} T_f)\right\} = \nabla \cdot (k_f \nabla T_f) + S_f \tag{3}$$

Energy–solid phase (porous matrix)

$$(\rho c_p)_s \frac{\partial T_s}{\partial t} = \nabla \cdot (k_s \nabla T_s) + S_s \tag{4}$$

where the subscripts f and s refer to fluid and solid phases, respectively. Here, T is the temperature, k_f and k_s are the fluid and solid thermal conductivities, respectively, c_p is the specific heat, and S is the heat generation term. If there is no heat generation either in the solid or in the fluid, one has $S_f = S_s = 0$.

Double-Decomposition of Variables

Macroscopic transport equations for turbulent flow in a porous medium are obtained through the simultaneous application of time and volume average operators over a generic fluid property φ. Such concepts are defined as follows.

$$\bar{\varphi} = \frac{1}{\Delta t}\int_t^{t+\Delta t} \varphi \, dt, \quad \text{with } \varphi = \bar{\varphi} + \varphi' \tag{5}$$

$$\langle\varphi\rangle^i = \frac{1}{\Delta V_f}\int_{\Delta V_f} \varphi\, dV; \quad \langle\varphi\rangle^v = \phi\langle\varphi\rangle^i; \quad \phi = \frac{\Delta V_f}{\Delta V}, \quad \text{with} \quad \varphi = \langle\varphi\rangle^i + {}^i\varphi \tag{6}$$

where ΔV_f is the volume of the fluid contained in a representative elementary volume (REV) ΔV, and intrinsic average and volume average are represented, respectively, by $\langle\ \rangle^i$ and $\langle\ \rangle^v$. The double decomposition idea, introduced and fully described in reference [31], combines Eqs. (5) and (6) and can be summarized as

$$\overline{\langle\varphi\rangle^i} = \langle\bar{\varphi}\rangle^i; \quad {}^i\bar{\varphi} = \overline{{}^i\varphi}; \quad \langle\varphi'\rangle^i = \langle\varphi\rangle^{i'} \tag{7}$$

and

$$\left.\begin{aligned}\varphi' &= \langle\varphi'\rangle^i + {}^i\varphi' \\ {}^i\varphi &= {}^i\bar{\varphi} + {}^i\varphi'\end{aligned}\right\} \quad \text{where } {}^i\varphi' = \varphi' - \langle\varphi'\rangle^i = {}^i\varphi - \overline{{}^i\varphi} \tag{8}$$

Therefore, the quantity φ can be expressed by either

$$\varphi = \overline{\langle\varphi\rangle^i} + \langle\varphi\rangle^{i'} + \overline{{}^i\varphi} + {}^i\varphi' \tag{9}$$

or

$$\varphi = \langle\bar{\varphi}\rangle^i + {}^i\bar{\varphi} + \langle\varphi'\rangle^i + {}^i\varphi' \tag{10}$$

The term ${}^i\varphi'$ can be viewed as either the temporal fluctuation of the spatial deviation or the spatial deviation of the temporal fluctuation of the quantity φ.

Macroscopic Flow Equations

When the average operators (5) and (6) are simultaneously applied over Eqs. (1) and (2), macroscopic equations for turbulent flow are obtained. Volume integration is performed over a representative elementary volume (REV) [34], resulting in

Continuity

$$\nabla\cdot\bar{\mathbf{u}}_D = 0 \tag{11}$$

where $\bar{\mathbf{u}}_D = \phi\langle\bar{\mathbf{u}}\rangle^i$ and $\langle\bar{\mathbf{u}}\rangle^i$ identifies the intrinsic (liquid) average of the time-averaged velocity vector $\bar{\mathbf{u}}$.

Momentum

$$\rho\left[\frac{\partial\bar{\mathbf{u}}_D}{\partial t} + \nabla\cdot\left(\frac{\bar{\mathbf{u}}_D\bar{\mathbf{u}}_D}{\phi}\right)\right] = -\nabla(\phi\langle\bar{p}\rangle^i) + \mu\nabla^2\bar{\mathbf{u}}_D - \nabla\cdot(\rho\phi\langle\overline{\mathbf{u}'\mathbf{u}'}\rangle^i) - \left[\frac{\mu\phi}{K}\bar{\mathbf{u}}_D + \frac{c_F\phi\rho|\bar{\mathbf{u}}_D|\bar{\mathbf{u}}_D}{\sqrt{K}}\right] \tag{12}$$

where the last two terms in Eq. (12) represent the Darcy and Forchheimer or form drags. The symbol K is the porous medium permeability, c_F is the form drag or

Forchheimer coefficient, $\langle \bar{p} \rangle^i$ is the intrinsic average pressure of the fluid, and ϕ is the porosity of the porous medium.

The macroscopic Reynolds stress, $-\rho\phi\langle\overline{\mathbf{u}'\mathbf{u}'}\rangle^i$, appearing in Eq. (12) is given as

$$-\rho\phi\langle\overline{\mathbf{u}'\mathbf{u}'}\rangle^i = \mu_{t_\phi} 2\langle\mathbf{D}\rangle^{\mathrm{v}} - \frac{2}{3}\phi\rho\langle k\rangle^i\mathbf{I} \tag{13}$$

where

$$\langle\mathbf{D}\rangle^v = \frac{1}{2}\left[\nabla(\phi\langle\bar{\mathbf{u}}\rangle^i) + [\nabla(\phi\langle\bar{\mathbf{u}}\rangle^i)]^T\right] \tag{14}$$

is the macroscopic deformation tensor, $\langle k\rangle^i = \langle\overline{\mathbf{u}'\cdot\mathbf{u}'}\rangle^i/2$ is the intrinsic turbulent kinetic energy, and μ_{t_ϕ} is the turbulent viscosity, which is modeled similarly to the case of clear flow, in the form

$$\mu_{t_\phi} = \rho f_\mu c_\mu \frac{\langle k\rangle^{i^2}}{\langle\varepsilon\rangle^i} \tag{15}$$

The intrinsic turbulent kinetic energy per unit mass and its dissipation rate are governed by the following equations.

$$\rho\left[\frac{\partial}{\partial t}\left(\phi\langle k\rangle^i\right) + \nabla\cdot\left(\bar{\mathbf{u}}_D\langle k\rangle^i\right)\right] = \nabla\cdot\left[\left(\mu + \frac{\mu_{t_\phi}}{\sigma_k}\right)\nabla\left(\phi\langle k\rangle^i\right)\right] - \rho\langle\overline{\mathbf{u}'\mathbf{u}'}\rangle^i{:}\nabla\bar{\mathbf{u}}_D + c_k\rho\frac{\phi\langle k\rangle^i|\bar{\mathbf{u}}_D|}{\sqrt{K}} - \rho\phi\langle\varepsilon\rangle^i \tag{16}$$

$$\rho\left[\frac{\partial}{\partial t}\left(\phi\langle\varepsilon\rangle^i\right) + \nabla\cdot\left(\bar{\mathbf{u}}_D\langle\varepsilon\rangle^i\right)\right] = \nabla\cdot\left[\left(\mu + \frac{\mu_{t_\phi}}{\sigma_\varepsilon}\right)\nabla\left(\phi\langle\varepsilon\rangle^i\right)\right] + c_1\left(-\rho\langle\overline{\mathbf{u}'\mathbf{u}'}\rangle^i{:}\nabla\bar{\mathbf{u}}_D\right)\frac{\langle\varepsilon\rangle^i}{\langle k\rangle^i} + c_2c_k\rho\frac{\phi\langle\varepsilon\rangle^i|\bar{\mathbf{u}}_D|}{\sqrt{K}} - c_2 f_\mu\rho\phi\frac{\langle\varepsilon\rangle^{i^2}}{\langle k\rangle^i} \tag{17}$$

where $\sigma_k = 1.4$, $\sigma_\varepsilon = 1.3$, $c_1 = 1.50$, $c_2 = 1.90$, $c_\mu = 0.09$, and $c_k = 0.28$ are nondimensional constants tuned for the low Reynolds number k-ε model, whereas f_2 and f_μ are damping functions, given by [36]

$$f_2 = \left\{1 - \exp\left[-\frac{(\nu\varepsilon)^{0.25}n}{3.1\nu}\right]\right\}^2 \times \left\{1 - 0.3\exp\left[-\left(\frac{(k^2/\nu\varepsilon)}{6.5}\right)^2\right]\right\} \tag{18}$$

$$f_\mu = \left\{1 - \exp\left[-\frac{(\nu\varepsilon)^{0.25}n}{14\nu}\right]\right\}^2 \times \left\{1 + \frac{5}{(k^2/\nu\varepsilon)^{0.75}}\exp\left[-\left(\frac{(k^2/\nu\varepsilon)}{200}\right)^2\right]\right\} \tag{19}$$

where n is the coordinate normal to the wall.

Macroscopic Energy Equation

Similarly, macroscopic energy equations are obtained for both fluid and solid phases by applying time and volume average operators to Eqs. (3) and (4). As in the flow case, volume integration is performed over a representative elementary volume (REV), resulting in

$$(\rho c_p)_f \left[\frac{\partial \phi \langle \overline{T_f} \rangle^i}{\partial t} + \nabla \cdot \left\{ \phi \left(\langle \bar{\mathbf{u}} \rangle^i \langle \overline{T_f} \rangle^i + \underbrace{\langle {}^i\bar{\mathbf{u}}^i \overline{T_f} \rangle^i}_{\text{thermal dispersion}} + \underbrace{\overline{\langle \mathbf{u}' \rangle^i \langle T_f' \rangle^i}}_{\text{turbulent heat flux}} + \underbrace{\langle \overline{{}^i\mathbf{u}'^i T_f'} \rangle^i}_{\text{turbulent thermal dispersion}} \right) \right\} \right]$$
$$= \underbrace{\nabla \cdot \left[k_f \nabla \left(\phi \langle \overline{T_f} \rangle^i \right) + \frac{1}{\Delta V} \int_{A_i} \mathbf{n}_i k_f \overline{T_f}\, dA \right]}_{\text{conduction}} + \underbrace{\frac{1}{\Delta V} \int_{A_i} \mathbf{n}_i \cdot k_f \nabla \overline{T_f}\, dA}_{\text{interfacial heat transfer}} \tag{20}$$

where the expansion

$$\langle \overline{\mathbf{u}_f'} \rangle^i = \overline{\langle (\langle \mathbf{u}' \rangle^i + {}^i\mathbf{u}')(\langle T_f' \rangle^i + {}^iT') \rangle^i} = \overline{\langle \mathbf{u}' \rangle^i \langle T_f' \rangle^i} + \langle \overline{{}^i\mathbf{u}'^i T_f'} \rangle^i \tag{21}$$

has been used in light of the double decomposition concept given by Eqs. (7)–(10) [32]. For the solid phase, one has

$$(\rho c_p)_s \left\{ \frac{\partial (1-\phi) \langle \overline{T_s} \rangle^i}{\partial t} \right\} = \underbrace{\nabla \cdot \left\{ k_s \nabla \left[(1-\phi) \langle \overline{T_s} \rangle^i \right] - \frac{1}{\Delta V} \int_{A_i} \mathbf{n}_i k_s \overline{T_s}\, dA \right\}}_{\text{conduction}}$$
$$\underbrace{- \frac{1}{\Delta V} \int_{A_i} \mathbf{n}_i \cdot k_s \nabla \overline{T_s}\, dA}_{\text{interfacial heat transfer}} \tag{22}$$

An interfacial heat transfer coefficient is needed when corresponding terms in Eqs. (20) and (22) are modeled following the local thermal nonequilibrium assumption [37]. Here, however, we assume local thermal equilibrium between the fluid and solid phases, i.e., we add Eqs. (20) and (22) and consider $\langle \overline{T_f} \rangle^i = \langle \overline{T_s} \rangle^i = \langle \overline{T} \rangle^i$, giving further

$$\left\{ (\rho c_p)_f \phi + (\rho c_p)_s (1-\phi) \right\} \frac{\partial \langle \overline{T} \rangle^i}{\partial t} + (\rho c_p)_f \nabla \cdot \left(\mathbf{u}_D \langle \overline{T} \rangle^i \right)$$
$$= \nabla \cdot \left\{ \left[k_f \phi + k_s (1-\phi) \right] \nabla \langle \overline{T} \rangle^i \right\} + \nabla \cdot \left[\frac{1}{\Delta V} \int_{A_i} \mathbf{n} \left(k_f \overline{T_f} - k_s \overline{T_s} \right) dS \right]$$
$$- (\rho c_p)_f \nabla \cdot \left[\phi \left(\langle {}^i\bar{\mathbf{u}}^i \overline{T_f} \rangle^i + \langle \overline{\mathbf{u}' T_f'} \rangle^i \right) \right] \tag{23}$$

The boundary conditions at A_i are given by

$$\left. \begin{array}{l} T_f = T_s \\ \mathbf{n} \cdot \left(k_f \nabla T_f \right) = \mathbf{n} \cdot \left(k_s \nabla T_s \right) \end{array} \right\} \quad \text{in } A_i \tag{24}$$

Equation (23) expresses the one-equation model for heat transport in porous media. Further, in view of Eq. (21), Eq. (23) can be rewritten as

$$\left\{\left(\rho c_p\right)_f \phi + \left(\rho c_p\right)_s (1-\phi)\right\} \frac{\partial \langle \overline{T} \rangle^i}{\partial t} + \left(\rho c_p\right)_f \nabla \cdot \left(\mathbf{u}_D \langle \overline{T} \rangle^i\right)$$
$$= \nabla \cdot \left\{\left[k_f \phi + k_s (1-\phi)\right] \nabla \langle \overline{T} \rangle^i\right\} + \underbrace{\nabla \cdot \left[\frac{1}{\Delta V} \int_{A_i} \mathbf{n} \left(k_f \overline{T_f} - k_s \overline{T_s}\right) dS\right]}_{I}$$
$$- \left(\rho c_p\right)_f \nabla \cdot \left[\phi \left(\underbrace{\overline{\langle \mathbf{u}' \rangle^i \langle T_f' \rangle^i}}_{II} + \underbrace{\langle {}^i\overline{\mathbf{u}}^i \overline{T_f} \rangle^i}_{III} + \underbrace{\langle \overline{{}^i\mathbf{u}'^i T_f'} \rangle^i}_{IV}\right)\right] \tag{25}$$

where to the underscored terms in Eq. (25), the following physical significance can be attributed.

1. Tortuosity based on microscopic time-average temperature.
2. Turbulent heat flux due to the fluctuating components of macroscopic velocity and temperature ($\langle \mathbf{u}' \rangle^i \langle T_f' \rangle^i = \langle \mathbf{u} \rangle^{i'} \langle T_f \rangle^{i'}$).
3. Thermal dispersion associated with deviations of microscopic time-average velocity and temperature. Note, that this term is also present when analyzing laminar convective heat transfer in porous media.
4. Turbulent thermal dispersion in a porous medium due to both time fluctuations and spatial deviations of both microscopic velocity and temperature.

In order to apply Eq. (25) to obtain the temperature field for turbulent flow in porous media, the underscored terms have to be modeled in some way as a function of the surface average temperature, $\langle \overline{T} \rangle^i$. To accomplish this, a gradient type diffusion model is used for all the terms, i.e., tortuosity (1), turbulent heat flux due to temporal fluctuations (2), thermal dispersion due to spatial deviations (3), and turbulent thermal dispersion due to temporal fluctuations and spatial deviations (4).

Using these gradient type diffusion models, we can write

Tortuosity

$$\left[\frac{1}{\Delta V} \int_{A_i} \mathbf{n} \left(k_f \overline{T_f} - k_s \overline{T_s}\right) dS\right] = \mathbf{K}_{\text{tor}} \cdot \nabla \langle \overline{T} \rangle^i \tag{26}$$

Turbulent heat flux

$$-\left(\rho c_p\right)_f \left(\phi \overline{\langle \mathbf{u}' \rangle^i \langle T_f' \rangle^i}\right) = \mathbf{K}_t \cdot \nabla \langle \overline{T} \rangle^i \tag{27}$$

Thermal dispersion

$$-\left(\rho c_p\right)_f \left(\phi \langle {}^i\overline{\mathbf{u}}^i \overline{T_f} \rangle^i\right) = \mathbf{K}_{\text{disp}} \cdot \nabla \langle \overline{T} \rangle^i \tag{28}$$

Turbulent thermal dispersion

$$-\left(\rho c_p\right)_f \left(\phi \langle^i \overline{\mathbf{u}'^i T'_f} \rangle^i\right) = \mathbf{K}_{\text{disp},t} \cdot \nabla \langle \overline{T} \rangle^i \tag{29}$$

For the above shown expressions, Eq. (25) can be rewritten as

$$\left\{\left(\rho c_p\right)_f \phi + \left(\rho c_p\right)_s (1-\phi)\right\} \frac{\partial \langle \overline{T} \rangle^i}{\partial t} + \left(\rho c_p\right)_f \nabla \cdot \left(\mathbf{u}_D \langle \overline{T} \rangle^i\right) = \nabla \cdot \left\{\mathbf{K}_{\text{eff}} \cdot \nabla \langle \overline{T} \rangle^i\right\} \tag{30}$$

where $\mathbf{K}_{\text{eff}}$ given by

$$\mathbf{K}_{\text{eff}} = \underbrace{[\phi k_f + (1-\phi) k_s]}_{k_{\text{eff}}} \mathbf{I} + \mathbf{K}_{\text{tor}} + \mathbf{K}_t + \mathbf{K}_{\text{disp}} + \mathbf{K}_{\text{disp},t} \tag{31}$$

is the effective overall conductivity tensor.

In order to be able to apply Eq. (30), it is necessary to determine the conductivity tensors in Eq. (31), i.e., $\mathbf{K}_{\text{tor}}$, $\mathbf{K}_t$, $\mathbf{K}_{\text{disp}}$, and $\mathbf{K}_{\text{disp},t}$. Following Kuwahara and Nakayama [38], this can be accomplished for the tortuosity and thermal dispersion conductivity tensors $\mathbf{K}_{\text{tor}}$ and $\mathbf{K}_{\text{disp}}$ by making use of a unit cell subjected to periodic boundary conditions for the flow and a linear temperature gradient imposed over the domain. The conductivity tensors are then obtained directly from the microscopic results (see reference [39] for detail). Nevertheless, for simplicity, the tortuosity and dispersion mechanisms are neglected here.

The turbulent heat flux and turbulent thermal dispersion terms $\mathbf{K}_t$ and $\mathbf{K}_{\text{disp},t}$, which cannot be determined from such a microscopic calculation, are modeled through the eddy diffusivity concept, similarly to Nakayama and Kuwahara [39]. It should be noticed that these terms arise only if the flow is turbulent, whereas the tortuosity and the thermal dispersion terms exist for both laminar and turbulent flow regimes.

The macroscopic version of the turbulent heat flux is given by

$$-\left(\rho c_p\right)_f \langle \overline{\mathbf{u}' T'_f} \rangle^i = \left(\rho c_p\right)_f \frac{\nu_{t_\phi}}{\sigma_T} \nabla \langle \overline{T}_f \rangle^i \tag{32}$$

where ν_{t_ϕ} is the macroscopic kinematic eddy viscosity whcih is related to the dynamic eddy viscosity given by Eq. (15) as $\mu_{t_\phi} = \rho \nu_{t_\phi}$ and σ_T is the turbulent Prandtl number.

According to Eqs. (21) and (32), the macroscopic heat flux due to turbulence is taken as the sum of the turbulent heat flux and the turbulent thermal dispersion found by Rocamora and de Lemos [32]. In view of the arguments given above, the sum of the conductivity tensors $\mathbf{K}_t$ and $\mathbf{K}_{\text{disp},t}$ is expressed as

$$\mathbf{K}_t + \mathbf{K}_{\text{disp},t} = \phi (\rho c_p)_f \frac{\nu_{t_\phi}}{\sigma_T} \mathbf{I} \tag{33}$$

4. NUMERICS

Equations (11), (12), and (30) subject to interface and boundary conditions were discretized in a two-dimensional control volume involving both clear and porous media. The finite-volume method was used in the discretization, and the

SIMPLE algorithm [40] was applied to handle the pressure-velocity coupling. The discretized form of the two-dimensional conservation equation for a generic property φ in steady-state regime reads,

$$I_e + I_w + I_n + I_s = S_\varphi \tag{34}$$

where I_e, I_w, I_n, and I_s represent, respectively, the fluxes of φ in the east, west, north, and south faces of the control volume and S_φ is term source.

Standard source term linearization is accomplished by using,

$$S_\varphi \approx S_\varphi^{**} \langle \varphi \rangle_p^i + S_\varphi^* \tag{35}$$

Discretization in the x-direction momentum equation gives,

$$S^{*x} = \left(S_e^{*x}\right)_P - \left(S_w^{*x}\right)_P + \left(S_n^{*x}\right)_P - \left(S_s^{*x}\right)_P + S_P^* \tag{36}$$

$$S^{**x} = S_\phi^{**} \tag{37}$$

where S^{*x} is the diffusive part, here treated in an explicit form. The second term, S^{**x}, entails the additional drag forces due to the porous matrix, the last two terms in Eq. (12), which are treated here explicitly.

5. RESULTS AND DISCUSSION

Input Parameters

For an impinging jet, the flow is considered to be turbulent for Reynolds number $\mathrm{Re} > 1000$, which is given by

$$\mathrm{Re} = \frac{\rho v_0 D_h}{\mu} \tag{38}$$

where v_0 is the incoming jet velocity and $D_h = B$ when calculating Re for adequate comparisons with similar simulations in the literature (see Figure 1).

The low Re turbulence model presented earlier was used in all simulation to follow. Also, in order to guarantee that grid nodes be positioned within the laminar sublayer, the closest grid node to the wall had a value for its wall coordinate y^+ less than unity ($y^+ \leq 1$). Further, inlet value for the turbulent kinetic energy k at the jet entrance was estimated using

$$k_0 = \frac{3}{2}(v_0 I)^2 \tag{39}$$

where I is the turbulence intensity assumed to prevail in the incoming flow. For the dissipation rate of k, ε, the inlet value was calculated according to

$$\varepsilon_0 = c_\mu^{3/4} \frac{k^{3/2}}{\ell} \tag{40}$$

Table 1. Input parameters for turbulent flow simulations

Fluid	Density ρ	Viscosity μ	B	L	T_0	T_1	Length scale, ℓ	Turbulence intensity, I
Air	$1.225\,\mathrm{kg/m^3}$	$1.789\times10^{-5}\,\mathrm{N\cdot s/m^2}$	14.23 mm	500 mm	309.1 K	347.6 K	0.07B	2%

where ℓ is a length scale associated with the energy containing eddies. Table 1 summarizes the parameters used as input.

Grid Independence Studies

Grid validation was conducted with the conditions $\mathrm{Re}=10{,}400$ and $H/B=2.6$. At the jet entrance, values in Table 1 were employed. For grid independence studies, the overall heat power at the impinged wall, given by

$$Q_w=\int_{x=o}^{x=L}-q''|_{y=H}w\,dx,\quad q''|_{y=H}=-k_f\frac{\partial\langle\overline{T}\rangle^i}{\partial y}\Bigg)_{y=H} \tag{41}$$

was calculated for several grids and compared in Table 2. In Eq. (41) $w=1$ m is the transverse plate width.

Also, local Nu number along that wall was evaluated by

$$\mathrm{Nu}=\frac{hH}{k_f}=\left(\frac{\partial\langle\overline{T}\rangle^i}{\partial y}\right)_{y=H}\frac{H}{T_1-T_0} \tag{42}$$

and h is a film coefficient. Figure 2*a* shows local Nu distribution calculated according to Eq. (42), alsoas a function of grid size. One can note in Table 2 that for grids greater than 80×216, the deviation for $\mathrm{Q_w}$ in relation to the finest grid is less than 0.5%. As such, all simulation for turbulent flow herein were carried out on a grid of size 80×216 which was refined close to the wall and about the jet entrance, where the steepest temperature gradients are expected to occur.

Clear Channel

The first set of results is related to the configuration shown in Figure 1*a*, where no porous material is attached to the bottom wall. Once an appropriate grid was chosen, code validation was carried out by comparing Nu numbers calculated at the bottom wall compared with results by Wang and Mujumdar [41], for two cases: namely, for $H/B=6$ and $\mathrm{Re}=5200$ (Figure 2*b*), and for $H/B=2.6$ and $\mathrm{Re}=10{,}400$ (Figure 2*c*). The figure indicates that for $H/B=6$ a good agreement is

Table 2. Influence of grid size on integral wall heat flux

Grid size	40×216	80×216	80×400	100×400
Wall heat power Q_w, Eq. (39)	772.75 W	818.87 W	825.68 W	820.05 W
Deviation in relation to grid 100×400	6.12%	0.14%	0.68%	0.00%

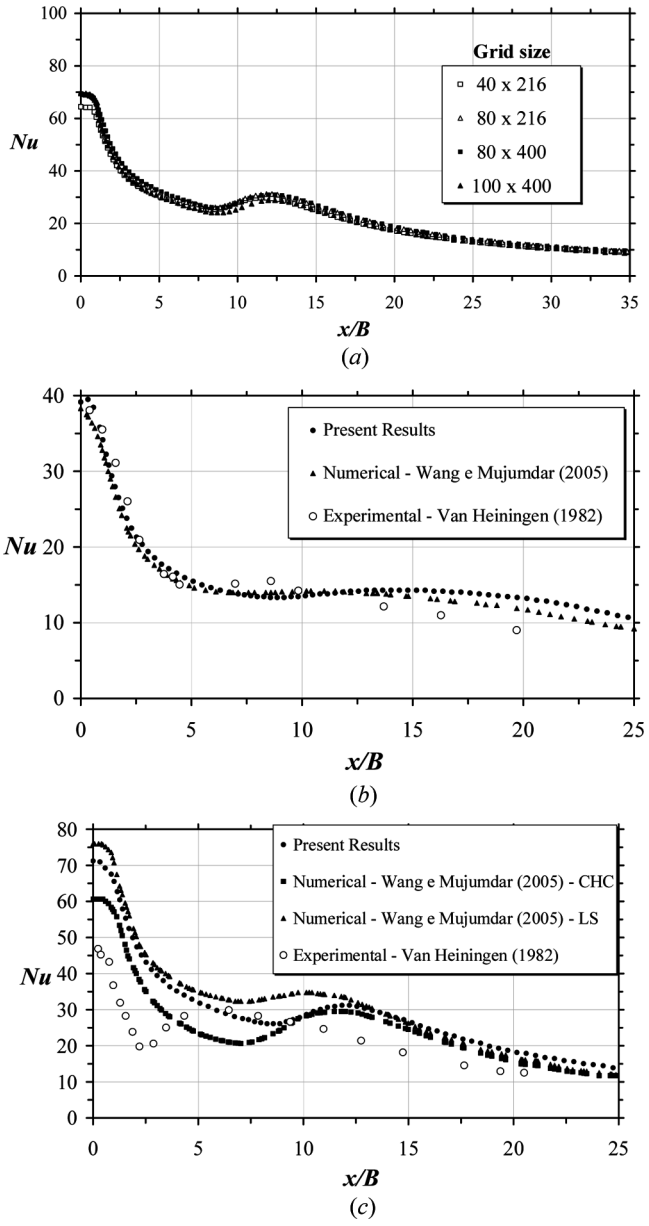

Figure 2. Validation for distribution of Nu along the lower plate for clear channel, Re = 10,400, $H/B = 2.6$. (*a*) Effect of grid size, (*b*) Re = 5200, $H/B = 6$, and (*c*) CHC = Chang et al., LS = Lauder and Sharma, see reference [41] for details.

obtained, whereas for $H/B = 2.6$ results do not match experimental values very well. This might be due to the fact that such flow entails a high degree of complexity, particularly for turbulent flow regime, as discussed by Wang and Mujumdar [41] and Heyerichs and Pollard [42]. Nevertheless, as the main purpose of this work is

to investigate the influence of a porous layer on heat transfer and not the turbulence model employed, and considering further the fact that a reasonable agreement with experimental data was achieved, the computer code and the grid size were assumed to be sufficiently accurate for the investigation here conducted.

Figure 3*a* shows streamlines for $H/B = 2.6$ as a function of Re, where one can note that the flow pattern is not substantially affected by Re, indicating that the fully turbulent regime is achieved. Further, the flow is characterized by a large

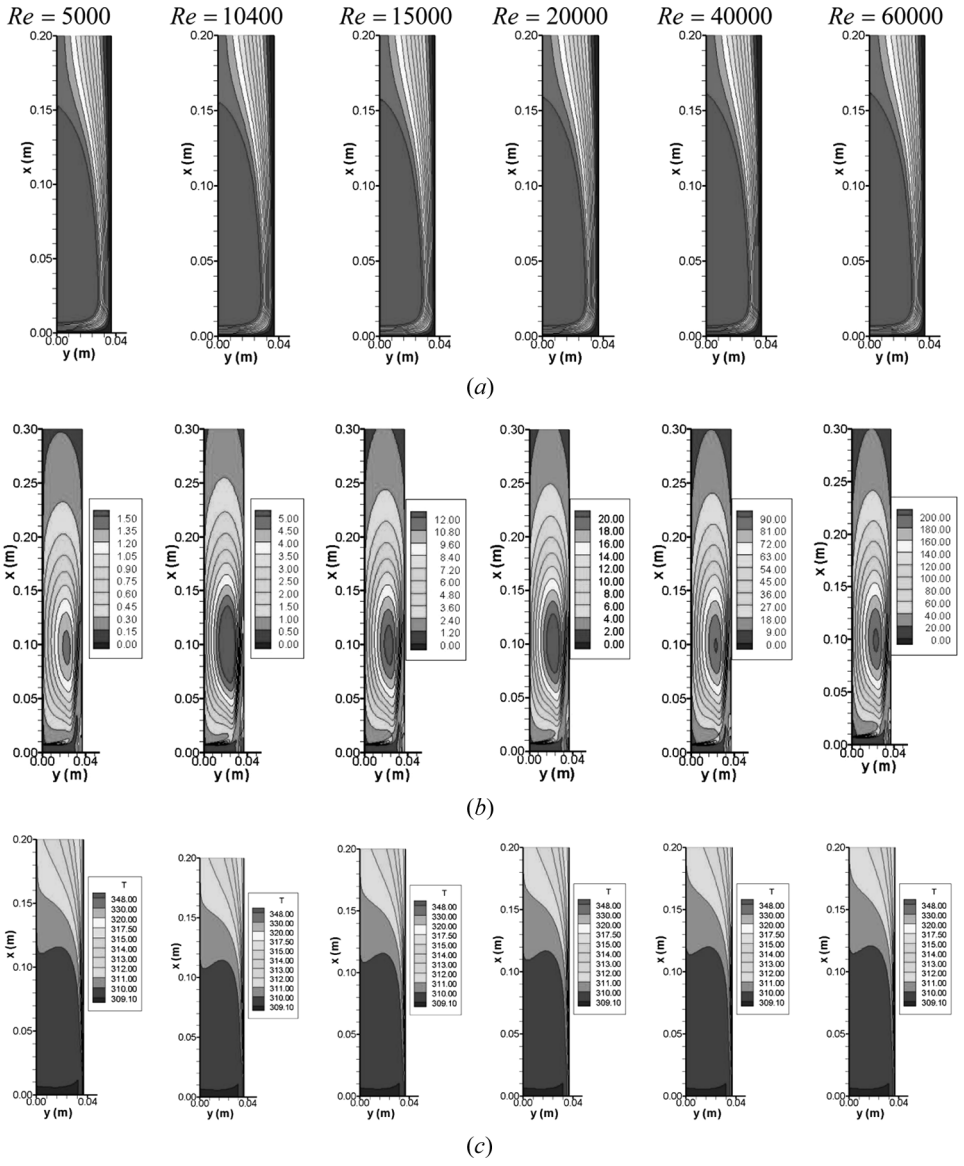

Figure 3. Effect of Re for $H/B = 2.6$. (*a*) Streamlines, (*b*) Turbulent kinetic energy k, and (*c*) Temperature T.

recirculation zone attached to the jet entrance, named primary vortex. Corresponding statistical field is presented in Figure 3*b*. In the figure one can note similarity among the maps and an increase on turbulence intensity as Re increases. Next, the temperature filed is presented in Figure 3*c*. Like the hydrodynamic field, no substantial changes are detected as Re increases. It is also observed that isolines are close to each other in the stagnation region, which characterizes a thin thermal boundary layer with high temperature gradients in that region.

For a performance analysis on heat transfer due to the jet velocity variation, Figure 4 shows the local Nu close to the target plate for various Reynolds numbers. According to Figure 4, as the Reynolds number increases, the curves for Nusselt shift toward higher values, increasing the peak at the stagnation region ($x = 0$). In addition, it can be seen that a second Nusselt peak appears for $\mathrm{Re} > 10{,}400$ and at about $x/B = 12$, becoming more pronounced as Re increases [33].

Channel with Porous Layer

When a layer of porous material is added to the bottom of the channel, the resulting configuration is shown in Figure 1*b*. The material is assumed to be rigid, with porosity ϕ, nondimensional thickness h/H, Darcy number $\mathrm{Da} = K/H^2$, and thermal conductivity ratio k_s/k_f. Results below are obtained using distinct values for such four parameters.

Effect of porosity, ϕ. In this section, the results were obtained using $H/B = 2.6$, $k_s/k_f = 10$, $\mathrm{Re} = 10{,}400$, $\mathrm{Da} = 8.95 \times 10^{-5}$, and $h/H = 0.50$.

Figure 5*a* shows streamlines and indicates that porosity variation does not strongly influences the flow behavior, as also confirmed by Graminho and de Lemos [30] and de Lemos and Fischer [33].

One can note that the presence of the porous layer reduces de size of the primary vortex, and that the strength of convection fluxes is smaller inside the porous material than in the clear passage, as expected. After the stagnation region, in the

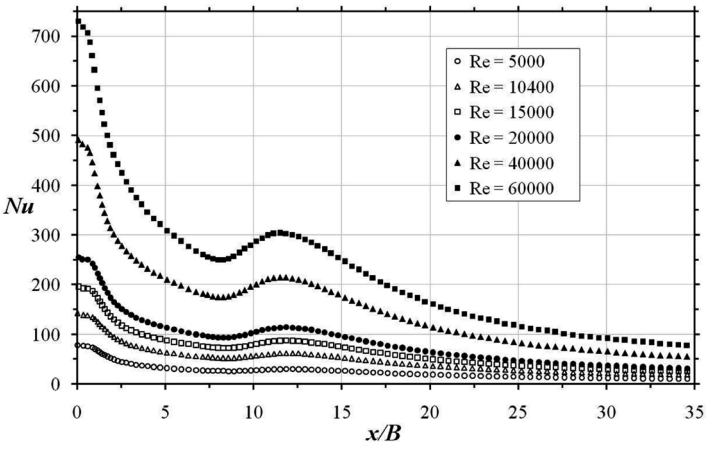

Figure 4. Effect of Re on Nu number for clear channel.

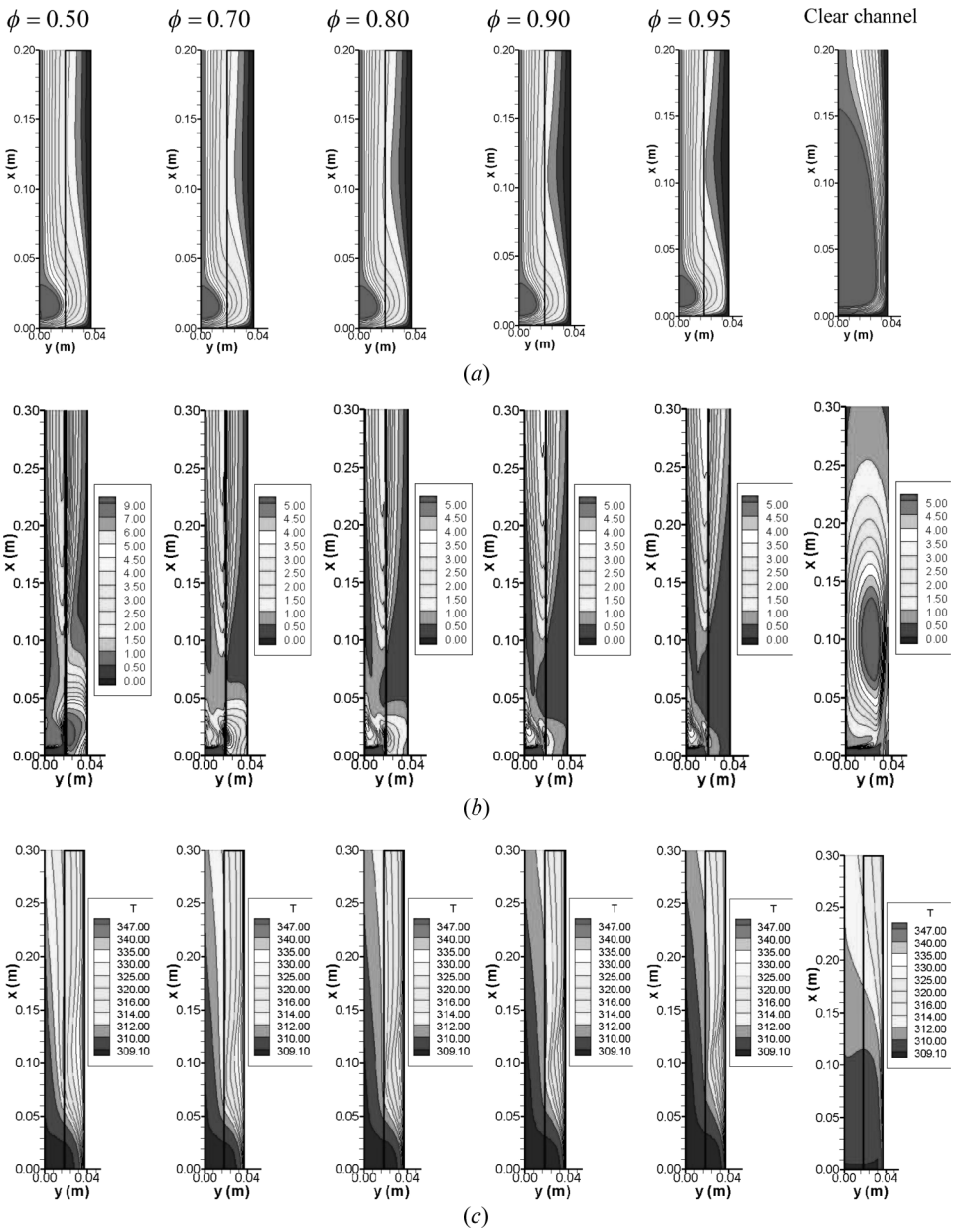

Figure 5. Effect of porosity ϕ for $H/B = 2.6$, $k_s/k_f = 10$, $\mathrm{Re} = 10{,}400$, $\mathrm{Da} = 8.95 \times 10^{-5}$, and $h/H = 0.50$. (*a*) Streamlines, (*b*) turbulent field k, and (*c*) temperature field T.

accelerating length ($0.06 < x < 0.10$) the flow tends to detach from the porous layer, reattaching further downstream. This trend is more pronounced as porosity increases, which is expected since within low porosity media the flow tends towards a plug-flow configuration, as it appears to be the case with $\phi = 0.50$.

Figure 5*b* shows corresponding results for the turbulent field. Note that as porosity decreases, k levels increase. High values of k are also encountered around the jet entrance where steep velocity gradients occur. Around the interface, levels of k are also high. This scenario contrasts with the clear channel distribution where most of the turbulence energy is generated in the recirculation zone corresponding to the primary vortex.

Porosity effects on T are presented in Figure 5*c*. In the figure, one can see that isolines present a coherent behavior with the flow pattern and, in the region $0.06 < x < 0.10$, such lines bulge away from the bottom wall. Further, it becomes evident that for low porosities the temperature is more homogenized and the thermal boundary layer becomes thicker, resulting in lower temperature gradients at the wall.

Nusselt numbers at wall are presented next in Figure 6, showing a peak in the stagnation region and a minimum value in the range $x/B = 5.0 - 10.0$, which is related to the above seen flow structure within $0.06 < x < 0.10$, where velocities are low and the boundary layer thick. Also, one can observe that porosity does not affect Nu in the stagnation region, but increases the Nusselt number for a higher ϕ as the flow downstream resembles a wall jet. For low porosities, the value for Nu downstream the flow is reduced and a minimum value for its longitudinal distribution tends to disappear, indicating that under such circumstances the temperature is more uniform, as already seen in Figure 5.

Effect of channel blockage, *h/H*. A study of the influence of the porous layer thickness in the heat transfer is now presented. The streamlines for a simulation with various porous layer thicknesses, with $H/B = 2.6$, $k_s/k_f = 10$, $\mathrm{Re} = 10{,}400$, $\mathrm{Da} = 8.95 \times 10^{-5}$, and $\phi = 0.90$, are presented in Figure 7*a*. The figure indicates that the value of h/H has a great influence on the flow pattern. As the blockage ratio increases, the primary vortex is reduced, being nearly extinguished for $h/H = 0.75$.

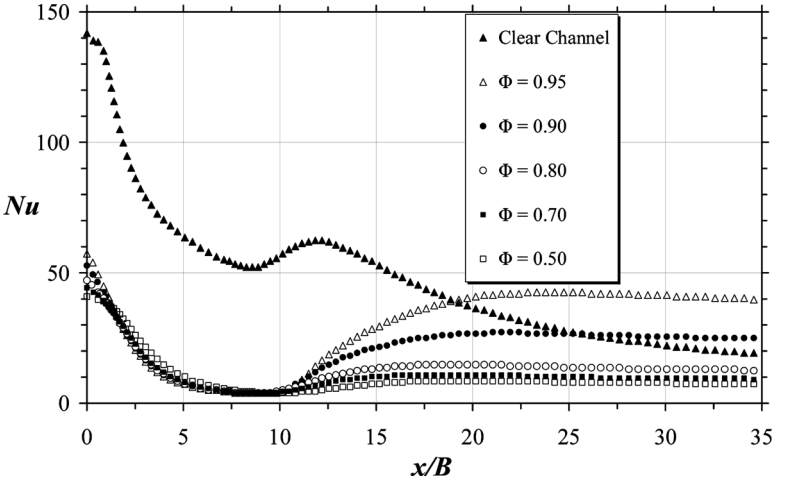

Figure 6. Local Nusselt distribution for various porosities with $H/B = 2.6$, $k_s/k_f = 10$, $\mathrm{Re} = 10{,}400$, $\mathrm{Da} = 8.95 \times 10^{-5}$, and $h/H = 0.50$.

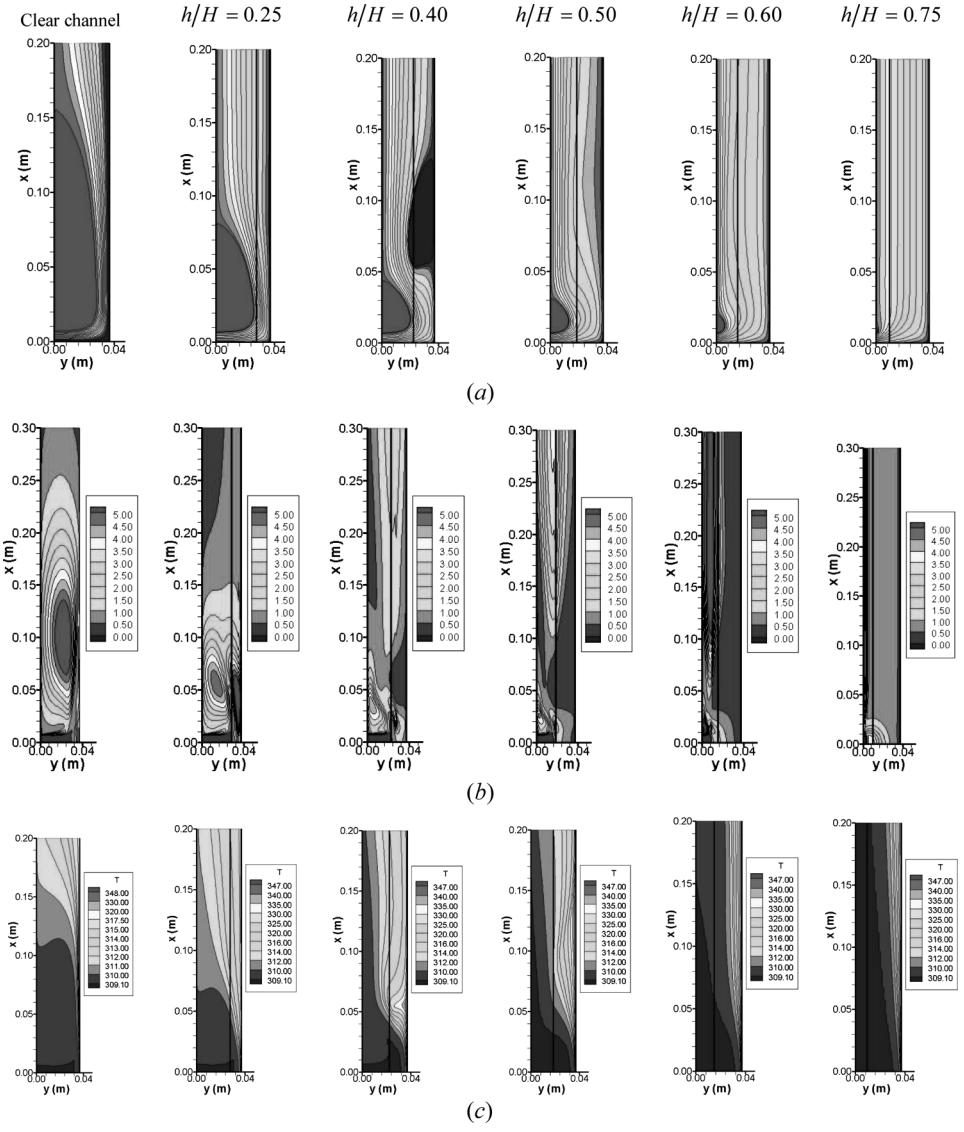

Figure 7. Effect of blockage ratio h/H for $H/B = 2.6$, $k_s/k_f = 10$, $\mathrm{Re} = 10{,}400$, $\mathrm{Da} = 8.95 \times 10^{-5}$, and $\phi = 0{,}90$. (*a*) Streamlines, (*b*) turbulent field k, and (*c*) temperature field T.

Specifically for $h/H = 0.40$, a new recirculation region seems to appear close to the bottom wall, whose vortex is named secondary. Also, as h/H increases, streamlines tend to become more uniform within the channel.

The corresponding statistical field behavior is presented in Figure 7*b*, where maps for k are shown. For h/H from 0.25 to 0.50, levels of k are reduced as the porous layer gets thicker. On the other hand for h/H higher than 0.60, steep velocity gradients in the fluid layer increases k since the fluid is pushed towards the free gap,

causing large velocity gradients in that regions. In addition, the temperature field in Figure 7*c* is also influenced by the porous layer thickness variation. The thermal field becomes more homogenized for thicker layers, as a consequence of the more uniform flow field observed in Figure 7*a*.

To complete the analysis, the local Nusselt number is presented in Figure 8 for various porous layer thicknesses. The stagnation Nusselt peak diminishes with the insertion of the porous layer, and for thicknesses less than $h = 0.40H$ the second peak in Nu is still present, as shown in Figure 8. The presence of the second peak is connected with the secondary vortices appearing in Figure 7. Also, it can be seen that variation of h/H does not influence the value of stagnation Nusselt peak as strongly as the variation of porosity, as can be concluded by comparing Figures 6 and 8. The main influence of the thickness of the porous layer is in the shape of the curve of Nusselt distribution along the stagnation region, changing from a double humped profile for clear channel to a single peak distribution for $h/H = 0.75$.

Effect of Darcy number, Da. Contrary to what was observed in the analysis of the effects of porosity, permeability strongly influences the hydrodynamic field, as can be seen in Figure 9*a*, which was calculated with $H/B = 2.6$, $k_s/k_f = 10$, $\mathrm{Re} = 10{,}400$, $\phi = 0.50$, and $h/H = 0.50$. The size of the primary vortex decreases with a decrease in permeability, as well as the fluid velocity inside the porous medium leading to a lower mass flow rate inside the layer covering the wall. For $\mathrm{Da} = 2.89 \times 10^{-6}$ and $\mathrm{Da} = 4.86 \times 10^{-7}$, from $x = 0.05\,\mathrm{m}$ to $x = 0.10\,\mathrm{m}$, the flow nearly vanishes in the porous material, as can be seen by the streamlines in Figure 9*a* and in the plots shown in Figure 10 for the velocity profiles along the axial channel position.

Back to the analysis of the previous figure, Figure 9*b* presents two-dimensional fields for the turbulence kinetic energy k. For $\mathrm{Da} = 7.30 \times 10^{-3}$ and

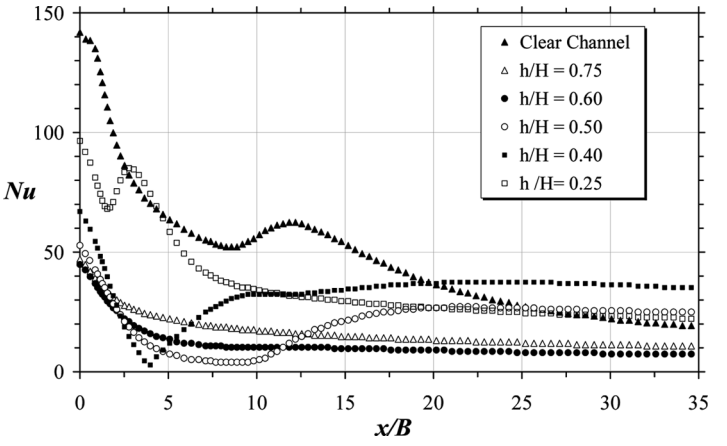

Figure 8. Local Nusselt distribution for various blockage ratios h/H with $H/B = 2.6$, $k_s/k_f = 10$, $\mathrm{Re} = 10{,}400$, $\mathrm{Da} = 8.95 \times 10^{-5}$, and $\phi = 0.90$.

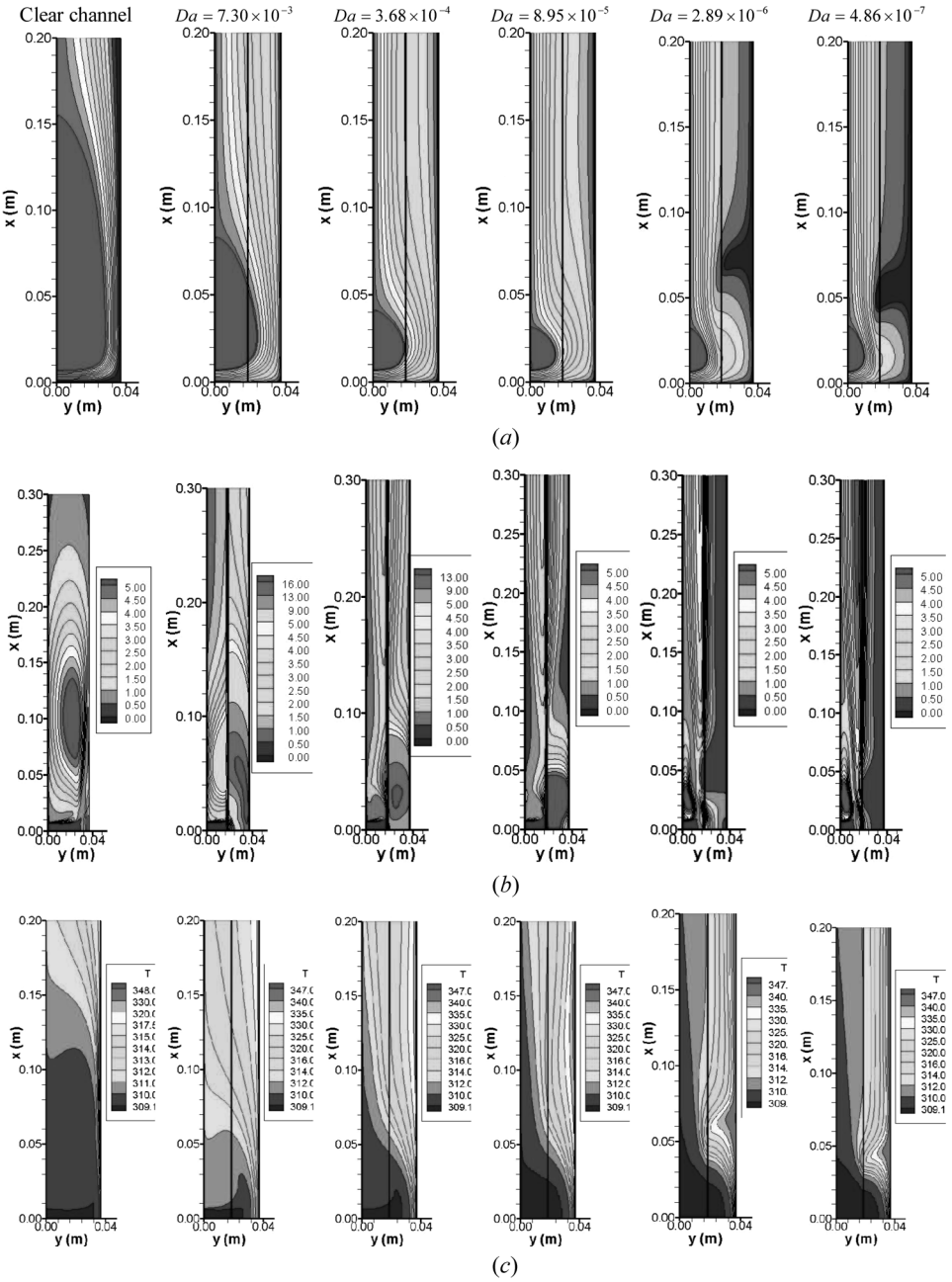

Figure 9. Effect of Da for $H/B = 2.6$, $k_s/k_f = 10$, $\mathrm{Re} = 10{,}400$, $\phi = 0.50$ e $h/H = 0.50$. (*a*) Streamlines, (*b*) turbulent field k, and (*c*) temperature field T.

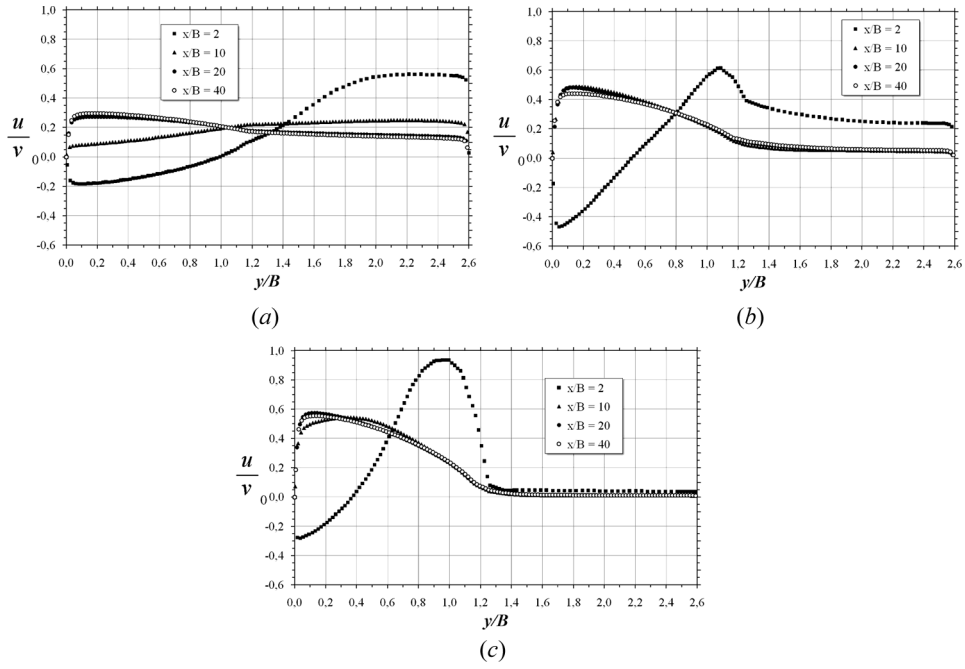

Figure 10. Velocity profiles at several axial stations for $H/B = 2.6$, $k_s/k_f = 10$, $\mathrm{Re} = 10{,}400$, $h/H = 0.50$. (*a*) $\mathrm{Da} = 7.30 \times 10^{-3}$, (*b*) $\mathrm{Da} = 8.95 \times 10^{-5}$, and (*c*) $\mathrm{Da} = 4.86 \times 10^{-7}$.

$\mathrm{Da} = 3.68 \times 10^{-4}$, generation of k is enhanced and is even grater than for the clear channel case. Again, the region of highest turbulence corresponds to the jet entrance region, where steep velocity gradients produce high generation rates of k. For vey low permeabilities, $\mathrm{Da} = 4.86 \times 10^{-7}$, and due to the fact that within the porous matrix velocities attain very low values, corresponding k values are also low. On the other hand, as fluid is pushed to flow thought the clear gap, higher values of k are found in that region.

Figure 9*c* shows temperature distributions for distinct values of $\mathrm{Da} = K/H^2$. In this figure, one can see that as permeability decreases, isothermal lines, referent to the highest temperatures, bulge from the hot wall thickening the thermal boundary layer at the surface. In accordance with the flow pattern (Figure 9*a*), cases with $\mathrm{Da} = 2.89 \times 10^{-6}$ and $\mathrm{Da} = 4.86 \times 10^{-7}$ present temperature peaks from $x = 0.05\,\mathrm{m}$ to $x = 0.10\,\mathrm{m}$, due to flow blockage in that region.

Figure 11 shows Nusselt numbers along the wall as a function of Da, where one can see that in such cases Nu at the stagnation region is most influenced, being reduced as Da is reduced. In the wall jet region, local Nu is also reduced, but less intensively when compared with its variation as a function of porosity (Figure 5).

Effect of thermal conductivity ration k_s/k_f. In this section the effect of varying k_s/k_f is investigated. Used parameters are $H/B = 2.6$, $\mathrm{Re} = 10{,}400$, $\mathrm{Da} = 8.95 \times 10^{-5}$, $\phi = 0.90$, $h/H = 0.50$, and several values of k_s/k_f. Evidently, since

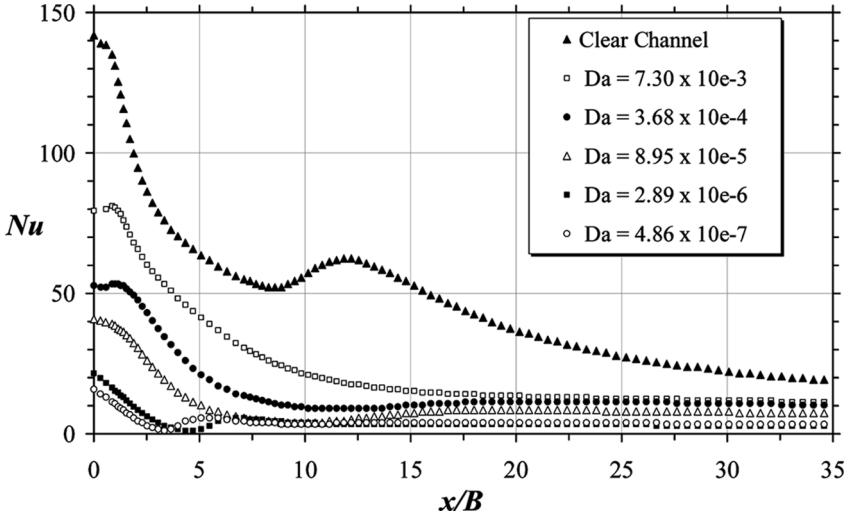

Figure 11. Local Nusselt distribution for various Da with $H/B = 2.6$, $k_s/k_f = 10$, $\mathrm{Re} = 10{,}400$, $\phi = 0.50$, and $h/H = 0.50$.

we are running only decoupled solutions, the flow filed is not impacted by the thermal conductivity ratio.

Figure 12 shows that, as expected, the thermal field is highly influenced by the ratio k_s/k_f. Fore high thermal conductivity ratios, isotherms depart from the hot wall indicating a reduction of temperature gradients and a thickening of the thermal boundary layer. Such observation is endorsed by Figure 13, which shows Nusselt at the hot wall. One can note that, in both the stagnation and along the wall regions, there is a substantial reduction of Nu as k_s/k_f increases. It is important to emphasize that tortuosity and dispersion are mechanisms neglected here, and that they might play a certain role when computing the temperature field. This is particularly important if one inspects Eq. (26) and sees that tortuosity is proportional to the difference between thermal conductivities.

Integral Wall Heat Flux

As pointed out by de Lemos and Fischer [33], another important parameter to evaluate the effectiveness in using porous layers is to calculate the integrated heat transferred from the bottom wall. Such overall heat transferred from the lower surface to the flowing fluid can be calculated for both configurations presented in Figure 1, as

$$q_w = \frac{1}{L}\int_o^L q_{w_x}(x)dx, \quad q_{wx} = -k_{\mathrm{eff}}\frac{\partial\langle T\rangle^i}{\partial y}\bigg|_{y=H},$$
$$k_{\mathrm{eff}} = \begin{cases} \phi k_f + (1-\phi)k_s & \text{with a porous layer} \\ k_f & \text{for clear channel} \end{cases} \tag{43}$$

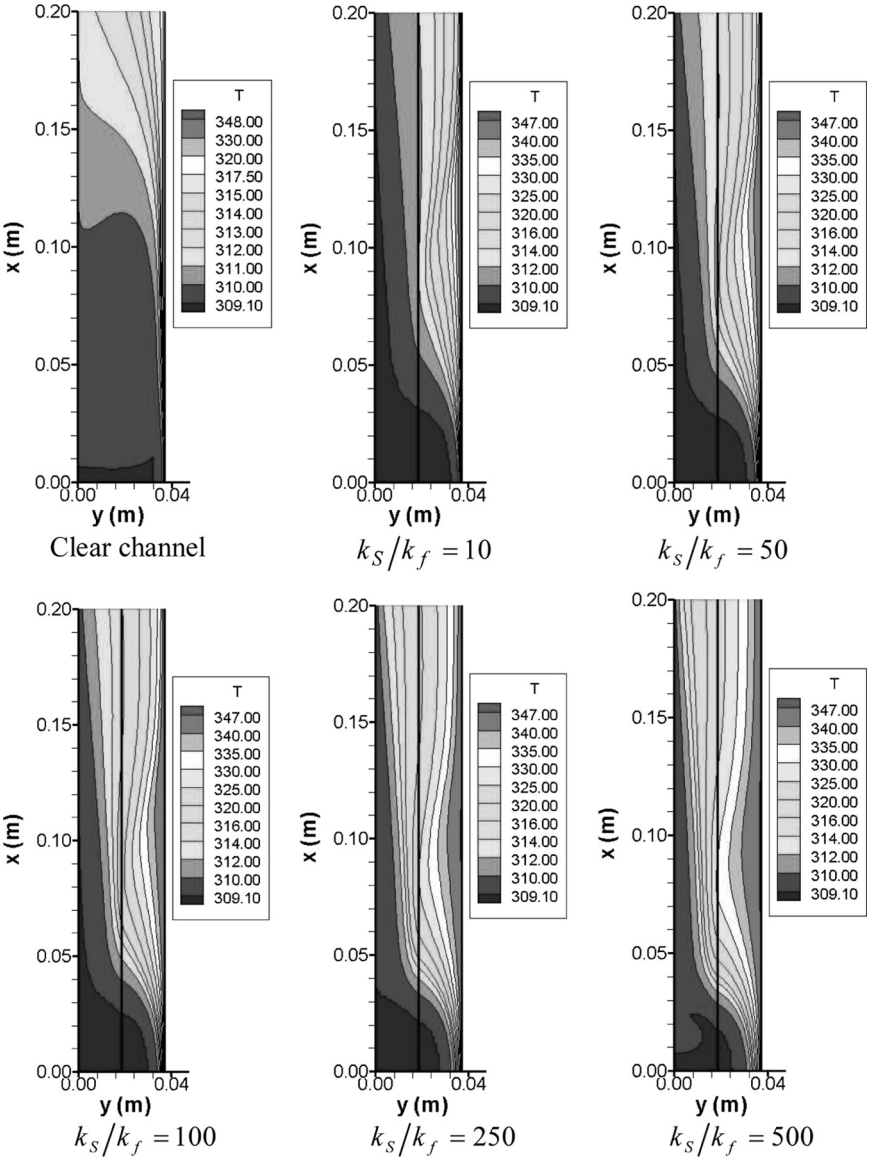

Figure 12. Effect of k_s/k_f on T, $H/B = 2.6$, $\mathrm{Re} = 10{,}400$, $\mathrm{Da} = 8.95 \times 10^{-5}$, $\phi = 0.90$, and $h/H = 0.50$.

For the cases where the a porous layer is considered, the wall hat flux is given a superscript ϕ in the form q_w^{ϕ}. The ratio $q^* = q_w^{\phi}/q_w$ can then be seen as a measure of the effectiveness of using a porous layer for enhancing or damping the amount of heat transferred through the wall.

Figure 14 compares the ratio $q^* = q_w^{\phi}/q_w$ as a function of ϕ for several Re, Da, and h/H, with $k_s/k_f = 10$. The figures suggest that for cases where there is more solid material per unit volume (low ϕ) and high permeabilities (high Da), there is a net

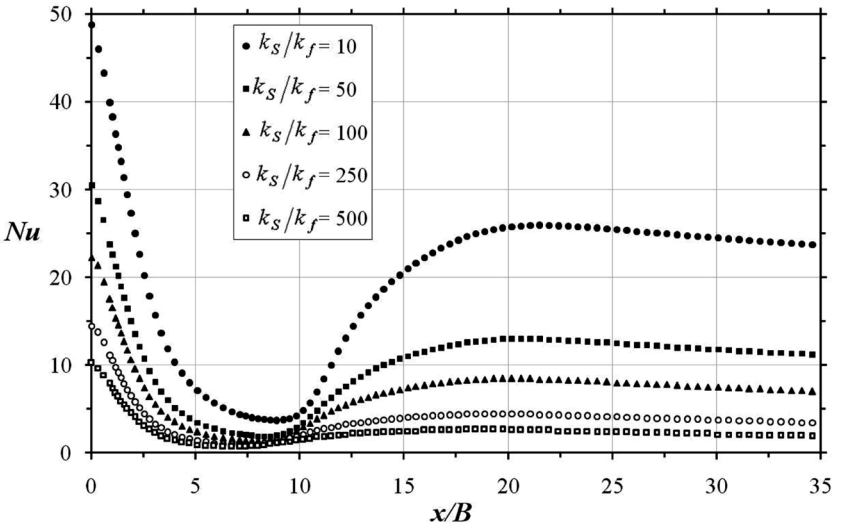

Figure 13. Local Nusselt distribution for various ratios k_s/k_f with $H/B = 2.6$, $\mathrm{Re} = 10{,}400$, $\mathrm{Da} = 8.95 \times 10^{-5}$, $\phi = 0.90$, and $h/H = 0.50$.

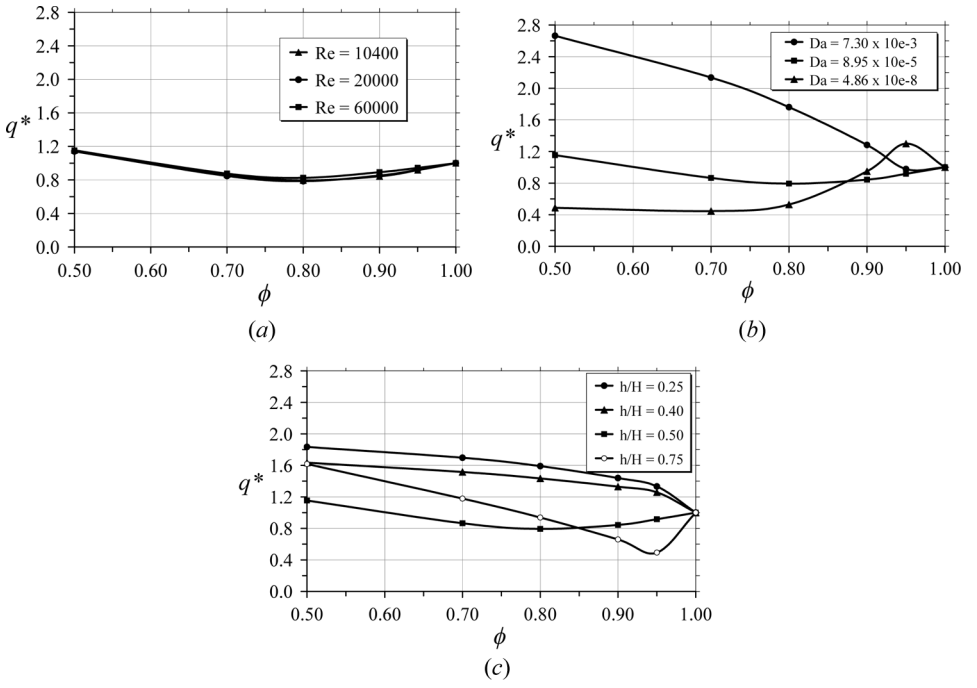

Figure 14. Integral heat flux ratio at the lower wall for varying porosity ϕ, $H/B = 2.6$, and $k_s/k_f = 10$. (*a*) Effect of Re, (*b*) effect of Da, and (c) effect of h/H.

gain when using a porous substrate covering the cooled wall ($q_w^{\phi}/q_w > 1$). This is more apparent as the layer gets ticker (Figure 14*c*). On the other hand, for high porosities ($\phi > 0.6$) and turbulent flow ($\mathrm{Re} > 10{,}000$), disruption of the thermal boundary layer close to the surface, due to the presence of a porous material, damps the overall heat transferred from the wall.

Figure 15 presents results for $q^* = q_w^{\phi}/q_w$ as a function of h/H for distinct ϕ and Da. Note that for low h/H or high Da, the use of a porous material is beneficial to heat transfer. Figure 16 further indicates that for less permeable materials, only cases with high porosity (Figure 16*a*) or thick layers (Figure 16*b*) give q_w^{ϕ}/q_w greater than unity. For more permeable media, a low porosity matrix gives better results, regardless of its thickness.

Finally, Figure 17 compiles results for q_w^{ϕ}/q_w when the conductivity ratio k_s/k_f is varied. Here, it is important to emphasize that results in the figure were obtained with the local thermal equilibrium (LTE) assumption ($\langle T \rangle^i = \langle T_f \rangle^i = \langle T_s \rangle^i$). Such

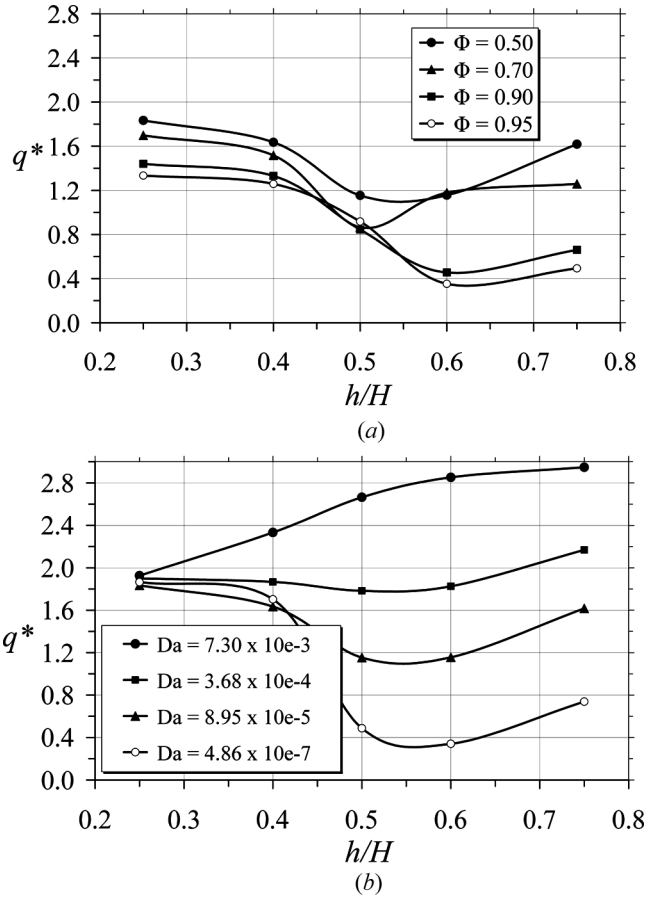

Figure 15. Integral heat flux ratio at the lower wall for varying blockage ratio h/H with $H/B = 2.6$, $k_s/k_f = 10$, $\mathrm{Re} = 10{,}400$ (*a*) $\mathrm{Da} = 8.95 \times 10^{-5}$, and (*b*) $\phi = 0.50$.

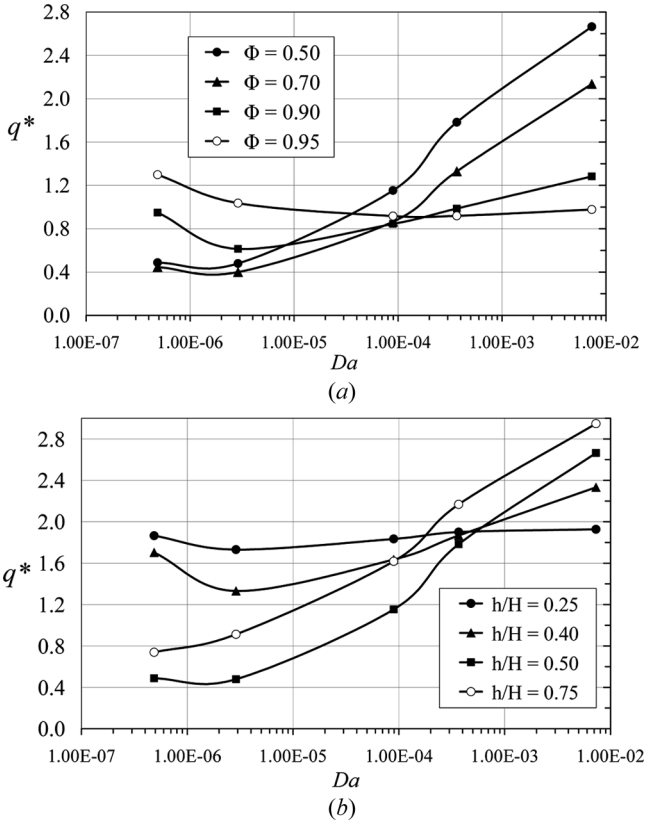

Figure 16. Integral heat flux ratio at the lower wall for various Da, $H/B = 2.6$, $k_s/k_f = 10$, Re = 10,400. (*a*) Effect of porosity ϕ, $h/H = 0.50$ and (*b*) effect of blockage ratio h/H, $\phi = 0.50$.

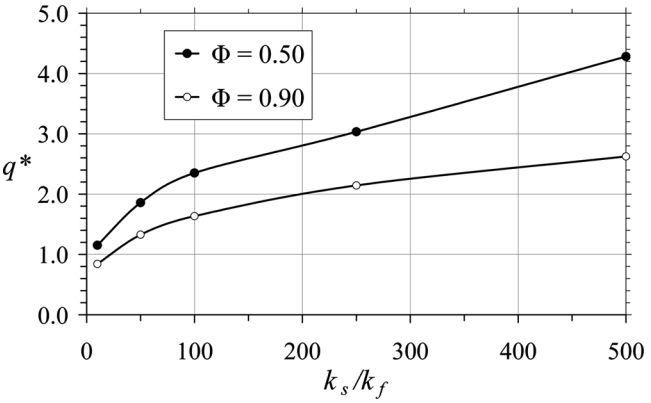

Figure 17. Integral heat flux ratio at the lower wall for various ratios k_s/k_f and porosities with Re = 10,400, $h/H = 0.5$, $H/B = 2.6$, and $\mathrm{Da} = 8.95 \times 10^{-5}$.

hypotheses might not be valid when the conductivity of the two media differs from each other by a large amount.

In Figure 17, one can note that increasing the conductivity ratio past $k_s/k_f > 10$, it is always possible to enhance the heat extracted from the bottom wall. The results herein might be useful to the design and analysis of energy efficient equipment.

6. CONCLUSION

The presence of a porous layer covering a surface where a jet collides eliminates the second peak in Nu and allows for controlling heat transfer from the wall. It was observed that porosity strongly influences the stagnation Nusselt value, while the porous layer thickness affects more intensely the distribution of Nu along the plate. Low porosity material tends to yield better heat absorption/release rates when compared with media that are more permeable. Increasing the thermal conductivity ratio is always beneficial to heat transfer enhancement form the hot wall. Ultimately, results in this work might be useful to engineers designing systems that make use of impinging jets over thermally-conducting porous materials, which possess a large interfacial air-to-solid contact area and are used advantageously for cooling or heating purposes.

REFERENCES

1. R. Gardon and J. C. Akfirat, Heat Transfer Characteristics of Impinging Two-Dimensional Air Jets, *J. Heat Transfer*, vol. 101, pp. 101–108, 1966.
2. E. M. Sparrow and T. C. Wong, Impinging Transfer Coefficients due to Initially Laminar Slot Jets, *Int. J. Heat and Mass Transfer*, vol. 18, pp. 597–605, 1975.
3. M. Chen, R. Chalupa, A. C. West, and V. Modi, High Schmidt Mass Transfer in a Laminar Impinging Slot Jet, *Int. J. Heat and Mass Transfer*, vol. 43, pp. 3907–3915, 2000.
4. V. A. Chiriac and A. Ortega, A Numerical Study of the Unsteady Flow and Heat Transfer in a Transitional Confined Slot Jet Impinging on an Isothermal Surface, *Int. J. Heat and Mass Transfer*, vol. 45, pp. 1237–1248, 2002.
5. Y. Zhang, X. F. Peng, and I. Conte, Heat and Mass Transfer with Condensation in Non-Saturated Porous Media, *Numer. Heat Transfer A*, vol. 52, pp. 1081–1100, 2007.
6. M. E. Taskin, A. G. Dixon, and E. H. Stitt, CFD Study of Fluid Flow and Heat Transfer in a Fixed Bed of Cylinders, *Numer. Heat Transfer A*, vol. 52, no. 3, pp. 203–218, 2007.
7. T. Basak, S. Roy, and H. S. Takhar, Effects of Nonuniformly Heated Wall(s) on a Natural-Convection Flow in a Square Cavity Filled with a Porous Medium, *Numer. Heat Transfer A*, vol. 51, no. 10, pp. 959–978, 2007.
8. J. Eriksson, S. Ormarsson, and H. Petersson, Finite-Element Analysis of Coupled Nonlinear Heat and Moisture Transfer in Wood, *Numer. Heat Transfer A*, vol. 50, no. 9, pp. 851–864, 2006.
9. V. Bubnovich, L. Henriquez, and N. Gnesdilov, Numerical Study of the Effect of the Diameter of Alumina Balls on Flame Stabilization in a Porous-Medium Burner, *Numer. Heat Transfer A*, vol. 52, no. 3, pp. 275–295, 2007.
10. X. B. Chen, P. Yu, S. H. Winoto, and H. T. Low, Free Convection in a Porous Wavy Cavity based on the Darcy-Brinkman-Forchheimer Extended Model, *Numer. Heat Transfer A*, vol. 52, no. 4, pp. 377–397, 2007.

11. N. Yucel and R. T. Guven, Forced-Convection Cooling Enhancement of Heated Elements in a Parallel-Plate Channels using Porous Inserts, *Numer. Heat Transfer A*, vol. 51, no. 3, pp. 293–312, 2007.
12. L. Betchen, A. G. Straatman, and B. E. Thompson, A Nonequilibrium Finite-Volume Model for Conjugate Fluid/Porous/Solid Domains, *Numer. Heat Transfer A*, vol. 49, no. 6, pp. 543–565, 2006.
13. Y. W. Zhang, Nonequilibrium Modeling of Heat Transfer in a Gas-Saturated Powder Layer Subject to a Short-Pulsed Heat Source, *Numer. Heat Transfer A*, vol. 50, no. 6, pp. 509–524, 2006.
14. C. R. Ruivo, J. J. Costa, and A. R. Figueiredo, Analysis of Simplifying Assumptions for the Numerical Modeling of the Heat and Mass Transfer in a Porous Desiccant Medium, *Numer. Heat Transfer A*, vol. 49, no. 9, pp. 851–872, 2006.
15. F. Moukalled and Y. Saleh, Heat and Mass Transfer in Moist Soil, Part I. Formulation and Testing, *Numer. Heat Transfer A*, vol. 49, no. 5, pp. 467–486, 2006.
16. X. H. Wang, M. Quintard, and G. Darche, Adaptive Mesh Refinement for One-Dimensional Three-Phase Flow with Phase Change in Porous Media, *Numer. Heat Transfer B*, vol. 50, no. 3, pp. 231–268, 2006.
17. X. H. Wang, M. Quintard, and G. Darche, Adaptive Mesh Refinement for One-Dimensional Three-Phase Flow with Phase Change in Porous Media, *Numer. Heat Transfer A*, vol. 50, no. 4, pp. 315–352, 2006.
18. A. Mansour, A. Amahmid, M. Hasnaoui, and M. Bourich, Multiplicity of Solutions Induced by Thermosolutal Convection in a Square Porous Cavity Heated from Below and Submitted to Horizontal Concentration Gradient in the Presence of Soret Effect, *Numer. Heat Transfer A*, vol. 49, no. 1, pp. 69–94, 2006.
19. A. V. Kuznetsov, L. Cheng, and M. Xiong, Effects of Thermal Dispersion and Turbulence in Forced Convection in a Composite Parallel-Plate Channel: Investigation of Constant Wall Heat Flux and Constant Wall Temperature Cases, *Numer. Heat Transfer A*, vol. 42, no. 4, pp. 365–383, 2002.
20. B. M. D. Miranda and N. K. Anand, Convective Heat Transfer in a Channel with Porous Baffles, *Numer. Heat Transfer A*, vol. 46, no. 5, pp. 425–452, 2004.
21. N. B. Santos and M. J. S. de Lemos, Flow and Heat Transfer in a Parallel-Plate Channel with Porous and Solid Baffles, *Numer. Heat Transfer A*, vol. 49, no. 5, pp. 471–494, 2006.
22. M. Assato, M. H. J. Pedras, and M. J. S. de Lemos, Numerical Solution of Turbulent Channel Flow Past a Backward-Facing-Step with a Porous Insert using Linear and Non-Linear k-ε Models, *J. Porous Media*, vol. 8, no. 1, pp. 13–29, 2005.
23. S. Y. Kim and A. V. Kuznetsov, Optimization of Pin-Fin Heat Sinks using Anisotropic Local Thermal Nonequilibrium Porous Model in a Jet Impinging Channel, *Numer. Heat Transfer A*, vol. 44, no. 8, pp. 771–787, 2003.
24. P. Xiang, A. V. Kunetsov, and A. M. Seyam, A Porous Medium Model of the Hydroentanglement Process, *J. Porous Media*, vol. 11, pp. 35–49, 2008.
25. P. Xiang and A. V. Kunetsov, Simulation of Shape Dynamics of a Long Flexible Fiber in a Turbulent Flow in the Hydroentanglement Process, *Int. Comm. Heat and Mass Transfer*, vol. 35, pp. 529–534, 2008.
26. M. Prakash, F. O. Turan, Y. Li, J. Manhoney, and G. R. Thorpe, Impinging Round Jet Studies in a Cilindrical Enclosure with and without a Porous Layer, Part I: Flow Visualizations and Simulations, *Chem. Eng. Sci.*, vol. 56, pp. 3855–3878, 2001a.
27. M. Prakash, F. O. Turan, Y. Li, J. Manhoney, and G. R. Thorpe, Impinging Round Jet Studies in a Cilindrical Enclosure with and without a Porous Layer, Part II: DLV Measurements and Simulations, *Chem. Eng. Sci.*, vol. 56, pp. 3879–3892, 2001b.

28. W.-S. Fu and H.-C. Huang, Thermal Performance of Different Shape Porous Blocks under an Impinging Jet, *Inter. J. Heat and Mass Transfer*, vol. 40, no. 10, pp. 2261–2272, 1997.
29. T.-Z. Jeng and S.-C. Tzeng, Numerical Study of Confined Slot Jet Impinging on Porous Metallic Foam Heat Sink, *Int. J. Heat and Mass Transfer*, vol. 48, pp. 4685–4694, 2005.
30. D. R. Graminho and M. J. S. de Lemos, Simulation of Turbulent Impinging Jet into a Cylindrical Chamber with and without a Porous Layer at the Bottom, *Int. J. Heat and Mass Transfer*, vol. 52, pp. 680–693, 2009.
31. M. J. S. de Lemos, *Turbulence in Porous Media: Modeling and Applications*, Elsevier, Kidlington, 2006.
32. F. D. Rocamora, Jr. and M. J. S. de Lemos, Analysis of Convective Heat Transfer of Turbulent Flow in Saturated Porous Media, *Int. Comm. Heat and Mass Transfer*, vol. 27, no. 6, pp. 825–834, 2000.
33. M. J. S. de Lemos and C. Fischer, Thermal Analysis of an Impinging Jet on a Plate with and without a Porous Layer, *Numer. Heat Transfer A*, vol. 54, pp. 1022–1041, 2008.
34. W. G. Gray and P. C. Y. Lee, On the Theorems for Local Volume Averaging of Multiphase System, *Int. J. Multiphase Flow*, vol. 12, pp. 401–410, 1977.
35. S. Whitaker, Advances in Theory of Fluid Motion in Porous Media, *Int. Eng. Chem.*, vol. 61, pp. 14–28, 1969.
36. K. Abe, Y. Nagano, and T. Kondoh, An Improved k-ε Model for Prediction of Turbulent Flows with Separation and Reattachment, *Trans. JSME Ser. B*, vol. 58, no. 554, pp. 3003–3010, 1992.
37. M. B. Saito and M. J. S. de Lemos, A Correlation for Interfacial Heat Transfer Coefficient for Turbulent Flow over an Array of Square Rods, *J. Heat Transfer*, vol. 128, pp. 444–452, 2006.
38. F. Kuwahara and A. Nakayama, Numerical Modeling of Non-Darcy Convective Flow in a Porous Medium, *Proc. 11th Int. Heat Transf. Conf.*, Kyongyu, Korea, vol. 4, pp. 411–416, 1998.
39. A. Nakayama and F. Kuwahara, A Macroscopic Turbulence Model for Flow in a Porous Medium, *J. Fluids Eng.*, vol. 121, pp. 427–433, 1999.
40. S. V. Patankar, *Numerical Heat Transfer and Fluid Flow*, Hemisphere, New York, 1980.
41. S. J. Wang and A. S. Mujumdar, A Comparative Study of Five Low Reynolds Number k-ε Models for Impingement Heat Transfer, *Appl. Therm. Eng.*, vol. 25, pp. 31–44, 2005.
42. K. Heyerichs and A. Pollard, Heat Transfer in Separated and Impinging Turbulent Flows, *Int. J. Heat Mass Transfer*, vol. 39, no. 12, pp. 2385–2400, 1996.